JOURNAL OF MATERIALS SCIENCE 26 (1991) 1401–1408

Oxidation sizing of iron and iron–neodymium–boron powders

M. STEWART, B. ROEBUCK, M. G. GEE
Division of Materials Metrology, National Physical Laboratory, Teddington, Middlesex TW11 OLW, UK

A powder sizing test developed for use on WC powders has been extended for use on iron and iron–neodymium–boron powders. In this test the particle size is derived from the rate of oxidation, because finer powders oxidize quicker. The rate of oxidation is monitored in a thermogravimetric analyser, where the powders are subjected to a controlled heating rate from room temperature to 1100 °C. If the constants from the Arrhenius law are known the powder size can be determined by comparing experimental oxidation plots with theoretical curves. For the sizing of a commercial spherical iron powder, the oxidation technique compared favourably with direct sizing using scanning electron microscopy and image analysis. The values for the activation energy of 125 kJ mol^{-1} determined in this study agree with previous studies. Validation of the sizing technique on a hydrogen-decrepitated stoichiometric $Nd_2Fe_{14}B$ powder proved difficult because it was not possible to determine a definitive size distribution independently. Metallography of partially oxidized samples showed that the process is two-stage, at low temperatures the neodymium oxidizes, and above 400 °C the powder behaves as pure iron. Theoretical curves based on one oxidation process with an activation energy of 100 kJ mol^{-1} gave the best fit to the experimental curves.

1. Introduction

Previous work on the isothermal oxidation of WC and TiC powders has shown that the particle size and size distribution can be determined from measurement of oxidation rate [1, 2]. Simply, finer powders oxidize more quickly due to their larger surface area to mass ratio. In the present work, this sizing method has been examined for application to the rare-earth based magnet material, $Nd_2Fe_{14}B$.

The oxidation behaviour of the $Nd_2Fe_{14}B$ powders was monitored in a thermogravimetric analyser, and for speed and convenience experiments were carried out isochronally. In isochronal experiments samples are subjected to a linear increase in temperature so that the complete reaction to oxide occurs more quickly than in isothermal experiments; however, theoretical analysis is more difficult. In order to perform the analysis and obtain powder size measurements it is necessary to understand the kinetics and mechanisms of the oxidation process and its temperature dependence, i.e. a rate equation and an activation energy. In contrast to the linear oxidation of WC powders, for $Nd_2Fe_{14}B$ the oxidation is parabolic, and activation energies of between 25 and 60 kJ mol^{-1} have been found [3, 4]. Previous oxidation sizing experiments on $Nd_2Fe_{14}B$ proved difficult without the accurate activation energy information [5]. Because the test has previously only been used for systems exhibiting linear behaviour, a supporting series of tests were additionally performed on pure iron powders to evaluate the technique on a model system.

2. Theory

Considering the inward growth of an oxide layer, thickness ξ_t, on a single-size spherical powder, initial radius r_1, an expression for the mass of powder, M'_t, at any time, t, is

$$M'_t \propto r_1^3 + D[r_1^3 - (r_1 - \xi_t)^3] \quad (1)$$

where D is the ratio of atomic weight of oxygen in the oxide to the initial atomic weight of metal.

Rearranging and dividing by the original mass, M_1, this gives

$$\frac{M_1(D + 1) - M'_t}{D M_1} = \frac{(r_1 - \xi_t)^3}{r_1^3} \quad (2)$$

The left-hand side of this expression is the normalized mass change during the oxidation, and all the experimental curves are plotted on this basis. The right-hand side of Equation 2 is used to determine the particle size by comparing theoretical curves using different r_1, with experimental data.

In order to calculate theoretical curves, an expression for the variation of thickness, ξ_t, with time and temperature is needed. For an isochronal experiment undergoing parabolic oxidation the rate equation is

$$(\xi_t)^2 = \int_0^t A_t dt \quad (3)$$

where A_t represents the Arrhenius law

$$A_t = \alpha_0 \exp\left[-\frac{Q}{R(T_0 + Ht)}\right] \quad (4)$$

and α_0 is a pre-exponential constant, Q the activation energy, R the gas constant, T_0 the starting temperature, and H the heating rate.

Equation 3 cannot be solved analytically, because the temperature is linearly dependent on the time. A simple numerical solution can be achieved by splitting the time into small equal intervals, δt, giving an expression for the oxide thickness at time t

$$\xi_t = (\xi_{t-1}^2 + A_t \delta t)^{1/2} \quad (5)$$

This expression can now be substituted into Equation 2. In practice it was found that dividing the time taken for the experiment into 200 intervals gave sufficient accuracy, and any further precision slowed computation.

The theoretical analysis outlined above has been based on the oxidation of a single size of powder. It can be readily expanded to accommodate a size distribution by taking a weighted average. Thus Equation 2 becomes

$$\frac{M_I(D+1) - M_t'}{D M_I} = \sum_0^j Mf_j \frac{(r_{Ij} - \xi_t)^3}{r_{Ij}^3} \quad \text{for } \xi_t \leq r_{Ij} \quad (6)$$

where Mf_j is the mass fraction of the jth population.

It is evident from Equations 4 to 6 that there are three unknowns for the prediction of the oxidation curves; the particle size distribution, the activation energy, and the pre-exponential factor. In order to use the method as a sizing technique, values for the activation energy and pre-exponential factor must be known. However, these are often not available. In the case of $Nd_2Fe_{14}B$ the values for Q in the literature for the activation energy differ markedly and α_0 values are not quoted. Alternatively, if the particle size distribution can be determined independently by another method, then this can be used to calculate the activation energy and pre-exponential factor. By comparing experimental and theoretical curves using the independently calibrated size distribution, values for Q and α_0 can be obtained by trial and error.

3. Experimental procedure

Isochronal experiments were performed on the powders in a Stanton Redcroft 780 thermogravimetric analyser (TGA). Weighed samples were placed in a platinum crucible and heated in still air to 1100 °C; this upper limit was set to inhibit any reactions with the platinum crucible. Temperature measurements were made using a thermocouple adjacent to the sample and were found to differ markedly from the nominal heating rates. The most frequently used nominal heating rates of 2.5, 5, 10 and 20 °C min^{-1} corresponded to average heating rates of approximately 2.2, 2.75, 7.9, and 18.0 °C min^{-1} over the range 20 to 1100 °C. The heating rates were calibrated by measuring the temperature throughout each experiment and the results were linearized using a least squares fit to give a starting temperature and average heating rate which was used for the theoretical curves. Because under different heating rates samples experience a particular temperature for differing times the mass change results were plotted against a time axis, where zero minutes corresponds to a temperature of 50 °C and not necessarily the start of the experiment.

In order to use the experiments as a particle sizing method it is important that the tests are quick and reproducible, and so a series of experiments were performed to investigate the effect of sample mass and heating rate, using nominal heating rates of 2.5, 5, 10 and 20 °C min^{-1} and varying nominal masses of 20, 40, 80 and 160 mg.

Most of the experiments were performed on a stoichiometric $Nd_2Fe_{14}B$ powder produced by hydrogen decrepitation followed by ball milling. A commercial 99.9% pure iron powder, nominally 6 to 9 μm diameter, was also examined.

Samples of the powders, before and after oxidation, were sprinkled on a carbon-filled adhesive for scanning electron microscopy (SEM) examination. Particle size analysis of the unoxidized iron powder was performed on the scanning electron micrographs using an image analysis system, because the particles were spherical and easily identifiable. However, because of the difficulty in separating the $Nd_2Fe_{14}B$ particles due to their irregular shape, it was not possible to size them using this method. Instead the powders were mounted in epoxy resin, sectioned, polished, and the true size distributions were calculated using the Schwartz–Saltykov method [6]. Windowless energy dispersive X-ray analysis was performed on the polished sections of partially and fully oxidized powders to monitor the progress of the reaction. X-ray diffraction of the powders was carried out on a Siemens D500 fitted with a secondary monochromator using Cu$K\alpha$ radiation.

4. Results and discussion

4.1. Effect of sample mass and heating rate

Fig. 1 shows the oxidation curves for the four different sample masses at a heating rate of 10 °C min^{-1}. It can be seen that for the higher masses the rate of reaction appeared to decrease after initially following a similar path to the 20 and 40 mg samples. For a given mass this change occurred at a fixed temperature, for all heating rates, and increasing the mass decreased the temperature at which this reduction in rate appeared. This apparent decrease is probably due to the formation of a protective crust, effectively sealing the bulk of the unoxidized powder from the atmosphere. For the highest heating rate 20 °C min^{-1} and the larger sample masses, 80 and 160 mg, the reaction became pyrophoric and the heating rate of the sample mass was non-linear in some regions. However, these are experimental artefacts linked to the size of the crucible, and for the purpose of particle sizing the most important thing to note is that the 20 and 40 mg results were almost identical. This indicated that under these conditions the experiment was reproducible and solely dependent on the powder particle size. It was found that for 20 mg samples heating rates up to 20 °C min^{-1} could be used.

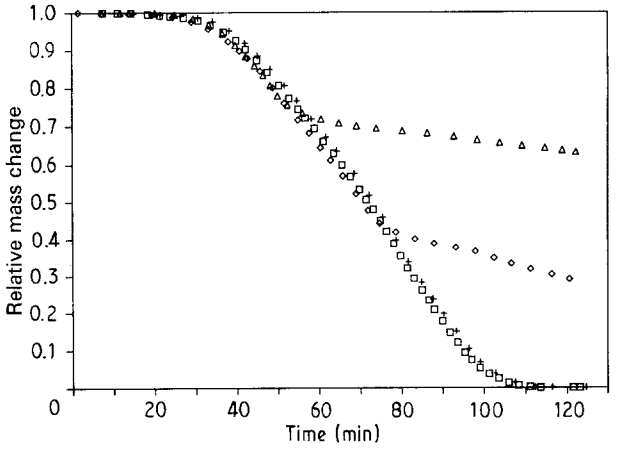

Figure 1 The effect of different sample masses on the isochronal curves at a heating rate of 10 °C min^{-1}. (□) 20 mg, (+) 40 mg, (◇) 80 mg, (△) 160 mg.

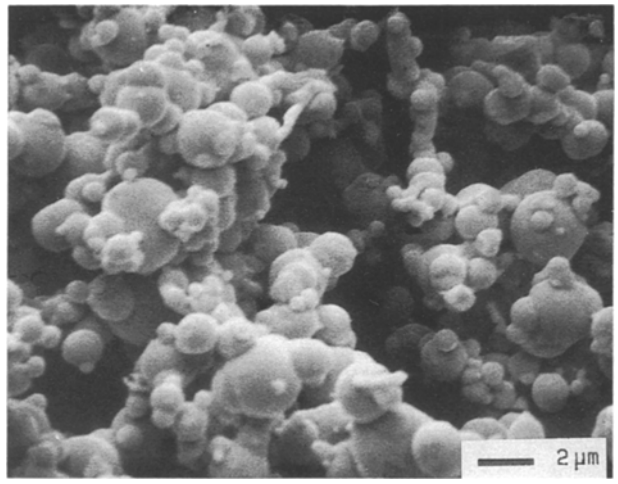

Figure 2 Scanning electron micrograph of commercial iron powder.

4.2. Sizing of iron powder

In order to test the particle theory on a parabolic system, initial tests were performed on iron powder. Fig. 2 shows that the particles are spherical, with a narrow distribution of sizes. Table I lists the results of particle sizing using image analysis on 337 particles, and have been converted into mass fractions assuming that each class can be represented by its mean radius. The distributions must be represented on a mass fraction basis because experimentally the technique is mass sensitive. Table I highlights the difference between distributions based on number fractions and those based on mass fractions for these powders. The class with the largest radius accounts for less than 2% of the number of particles yet almost 15% of the mass, and the smallest radius class represents more than 12% of the number yet less than 0.3% of the mass. The distribution was initially divided into ten classes; however, because additional classes slow computation of the theoretical curves and the repeatability of the experiments was not better than 2%, classes containing less than 5% of the mass were rounded into the adjacent class.

TABLE I Size distribution of iron powder from image analysis

Radius (μm)	Number	Number fraction	Mass fraction
0.37	41	0.12	0.003
0.62	62	0.18	0.020
0.86	71	0.21	0.065
1.10	52	0.16	0.100
1.35	44	0.13	0.155
1.59	30	0.09	0.175
1.84	20	0.06	0.178
2.08	8	0.023	0.104
2.32	3	0.009	0.054
2.57	6	0.018	0.146

As discussed the method must first be "calibrated" by determining the activation energy and pre-exponential factor using a powder of a known distribution. By systematically varying the Q and α_0, a series of theoretical curves can be compared with the experimental data until a best fit is obtained. Fig. 3 shows the effect on the theoretical curves of varying Q and α_0 from the base values of $Q = 125\ kJ\ mol^{-1}$ and $\alpha_0 = 5 \times 10^6\ \mu m^2\ min^{-1}$, using the powder size data in Table I and a heating rate of 7.84 °C min^{-1}. Increasing Q by 8% moves the curve to the right (decreasing the oxidation rate), and decreasing by 8% produces a similar shift to the left. From the form of the Arrhenius law (Equation 4) it is evident that the value of Q determines at what temperature significant reaction takes place, and this is reflected in the linear relationship between changing Q and the shift in the curve along the x-axis. In contrast the curves are largely insensitive to change in α_0, doubling the value produces a relatively small shift towards faster oxidation, and halving α_0 gives a similar shift to the right.

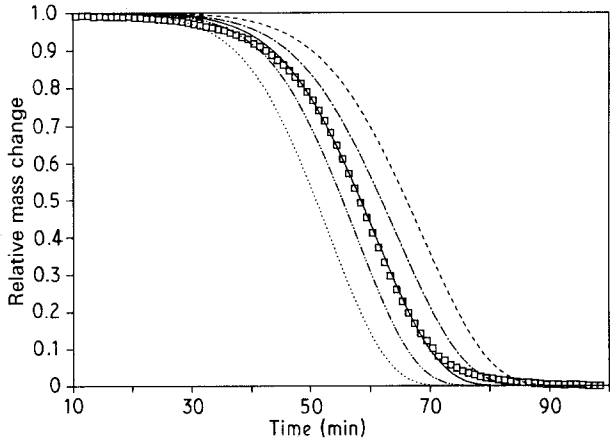

Figure 3 Theoretical curves showing the effect of varying Q and α_0. Isochronal heating rate of 10 °C min^{-1}. Q (kJ) and α_0 values, respectively: (—) 125, 5×10^6, (– – –) 135, 5×10^6, (. . .) 115, 5×10^6, (— · · · —) 125, 1×10^7, (— · — ·—) 125, 2.5×10^6.

From this it is apparent that similar curves can be produced by altering both Q and α_0 in the same manner; however, this will affect the overall slope of the curve. As both Q and α_0 are increased the rate of oxidation increases and the slope of the curve increases. Conversely, as Q and α_0 are decreased the curve becomes flatter, the low Q implies the reaction starts at a lower temperature and, coupled with a low α_0, a slow oxidation rate. Although the exact deviation due to modifying Q and α_0 is highly dependent

on the other parameters, particle size, heating rate and starting temperature, the general trends discussed are useful in curve fitting for Q and α_0 determination. Fig. 4 shows the experimental curves for a 20 mg sample mass at nominal heating rates of 10 and 20 °C min^{-1}, and theoretical best fits using the powder size data from Table I and values of 125 kJ mol^{-1} for Q, and 5×10^6 μm^2 min^{-1} for α_0. It is important to note that the best fit was performed on only one test, the slower heating rate, and the fact that there is good agreement at the faster heating rate indicates the consistency of the theoretical approach. The data could equally well have been used to determine the size distribution using the values of Q and α_0 already obtained.

Upon closer examination of the curves at the beginning and end of the experiment, it can be seen that there are slight differences between theory and experiment which cannot be accommodated by adjusting the Q and α_0. These discrepancies could be accounted for by errors in the SEM particle sizing. Fig. 5 shows the theoretical curves for two size distributions, one with the radius of each class 25% larger, and one 25% smaller than the SEM derived distribution. Although a $\pm$ 25% error may seem large it must be noted that the distribution was obtained from only 337 particles. In contrast, for the oxidation sizing technique, assuming a single size of 3 μm, there are of the order of 10^7 particles examined in a 20 mg sample.

As a final check on the validity of the theory, the activation energy derived here compares favourably with previous work on iron oxidation, in the range 500 to 1100 °C, where a Q of 138 kJ mol^{-1} was obtained [7].

4.3. Sizing of $Nd_2Fe_{14}B$ powder

The $Nd_2Fe_{14}B$ powders examined had a much wider size distribution and were irregularly shaped in comparison with the iron powder. Fig. 6 shows a scanning electron micrograph of the powder, and Table II lists the particle size distribution derived from image analysis on optical cross-sections of 2075 particles. In an attempt to obtain a more uniform size distribution the powder was dry sieved first through 45 μm and then 20 μm stainless steel square hole meshes. The oxidation curves for sieved and as-received powders are much broader than those from the iron powders (Fig. 7). As expected the as-received and sieved curves were identical at the start, because the fines are not affected, and only at the end of the experiment did the sieved curve finish sooner, as a greater number of large particles have been excluded. This shows both the reproducibility, and the potential of the technique for

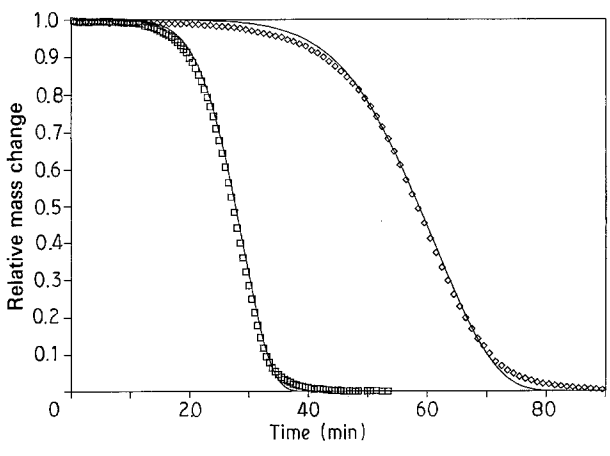

Figure 4 Experimental and theoretical curves on iron powder for heating rates of (◇) 7.8 and (□) 17.8 °C min^{-1}.

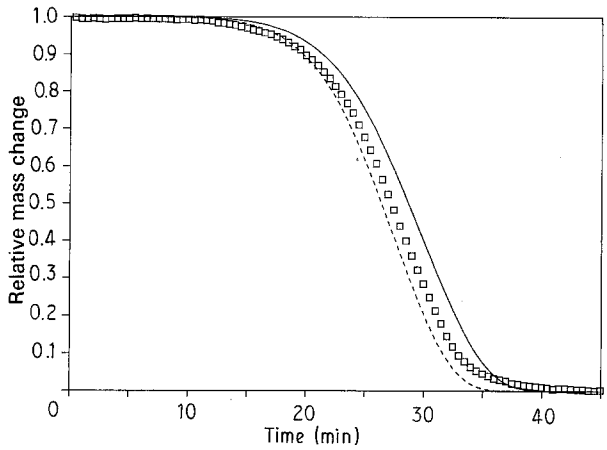

Figure 5 Theoretical curves incorporating a specified uncertainty in the iron powder particle size with a heating rate of 20 °C min^{-1}. Error: (—) + 25%, (– –) – 25%.

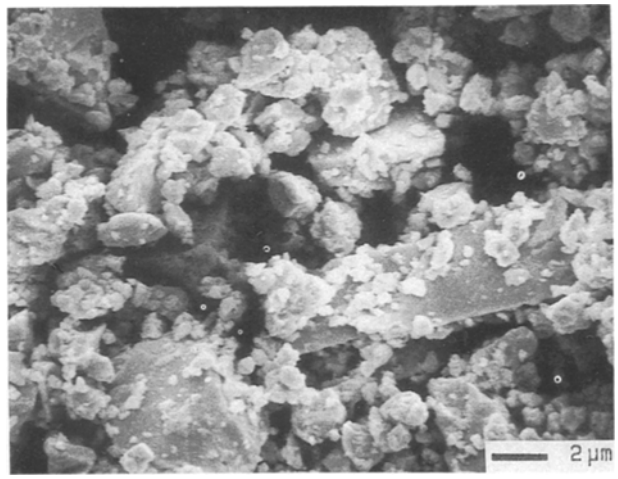

Figure 6 Scanning electron micrograph of $Nd_2Fe_{14}B$ powder.

TABLE II Size distribution of $Nd_2Fe_{14}B$ powder from image analysis of cross-sections

Radius (μm)	Number	Number fraction	Number[a] fraction	Mass fraction
2.52	1708	0.82	0.912	0.40
4.44	222	0.11	0.063	0.15
6.37	70	0.03	0.014	0.10
8.29	37	0.02	0.006	0.10
10.21	14	0.01	0.002	0.05
12.13	12	0.005	0.002	0.07
14.05	8	0.005	0.001	0.08
15.97	2	<0.001	<0.001	0.02
17.90	1	<0.001	<0.001	0.01
19.82	1	<0.001	<0.001	0.02

[a] Number fraction adjusted using the Schwartz–Saltykov method [6].

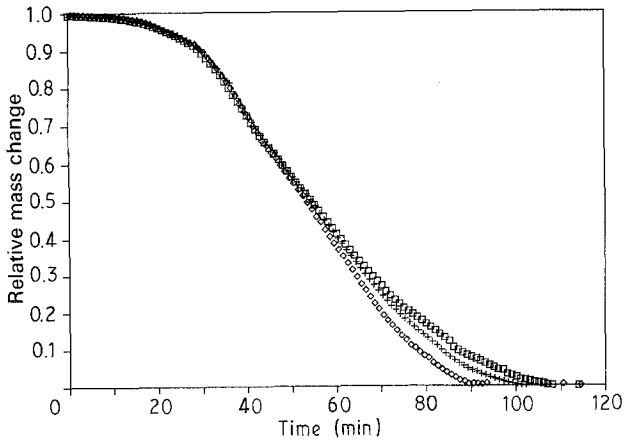

Figure 7 Isochronal curves for (□) as-received and (+ , ◇) sieved $Nd_2Fe_{14}B$ powders. (+) 45 μm sieve, (◇) 20 μm sieve.

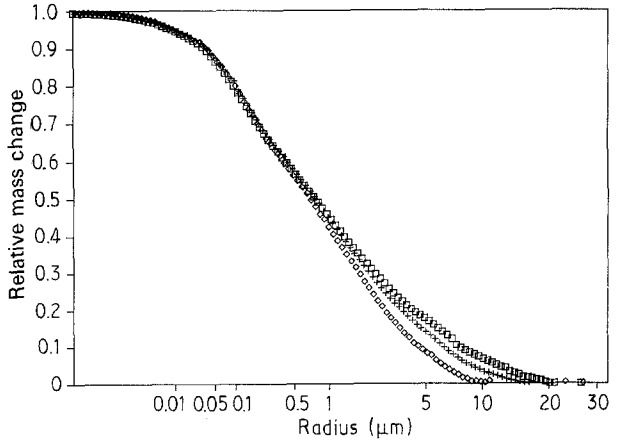

Figure 9 Experimental curves for $Q = 100\ kJ\ mol^{-1}$ and $\alpha_0 = 1 \times 10^6\ \mu m^2\ min^{-1}$. (□) As-received, (+) 45 μm sieve, (◇) 20 μm sieve.

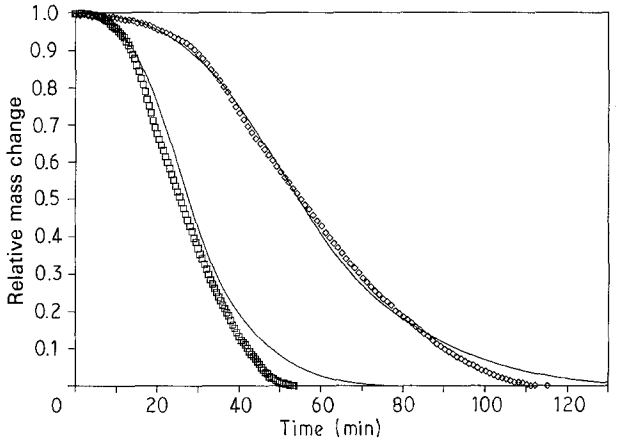

Figure 8 Experimental and theoretical curves on as-received $Nd_2Fe_{14}B$ powders for heating rates of (◇) 7.8 and (□) 17.8 °C min^{-1}. $Q = 50\ kJ\ mol^{-1}$ and $\alpha_0 = 300\ \mu m^2\ min^{-1}$.

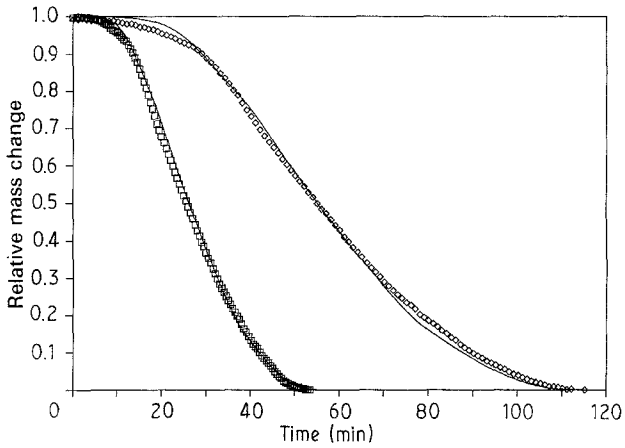

Figure 10 Experimental and theoretical curves on as-received $Nd_2Fe_{14}B$ powders for heating rates of (◇) 7.8 and (□) 17.8 °C min^{-1}. $Q = 100\ kJ\ mol^{-1}$ and $\alpha_0 = 1 \times 10^6\ \mu m^2\ min^{-1}$.

qualitatively "fingerprinting" powders. However, for quantification, the oxidation rate of the material must first be determined. The oxidation rate parameters were found using the particle size distribution from the image analysis to produce curves for comparison with the 10 °C min^{-1} experiment. By this method, values of 50 kJ mol^{-1} and 300 $\mu m^2\ min^{-1}$ were found for the activation energy and a pre-exponential factor, respectively. However, when using other heating rates the fit between experiment and theory is not so good (Fig. 8).

Q and α_0 were also determined by another technique using particle size information from the sieving experiments. Assuming that the particles were spherical, the maximum particle size for the sieved samples must have been equal to the sieve size, but only if the oxidation curve for the sieved powder was different to that of the as-received powder. Because the largest particles oxidize the slowest, the point where the normalized mass curves cut the x-axis corresponded to the maximum detectable particle size of the batch. Thus, for a given set of oxidation rate parameters the x-axis can be annotated to indicate the completion of oxidation of a given particle size. The x-axis in Fig. 9 has been annotated in this manner and the values of Q and α_0 which gave the best agreement in the oxidation

TABLE III Size distribution obtained from oxidation sizing, using Q and α_0 from sieve analysis

Radius (μm)	Mass fraction
0.1	0.1
0.5	0.1
1	0.1
2	0.1
5	0.1
6	0.1
8	0.1
20	0.1
25	0.1
30	0.1

experiments on the sieved powders were 100 kJ mol^{-1} and $1 \times 10^6\ \mu m^2\ min^{-1}$, respectively. Having established Q and α_0, the complete size distribution for the unsieved powder can now be determined. A reasonable fit was obtained for both heating rates (Fig. 10), and the size distribution is listed in Table III. Although the mean particle sizes determined by the two methods, image analysis (Table II) and oxidation sizing (Table III), are similar, the distribution determined by image analysis was much narrower. There

are two possible reasons for this; firstly, the uncertainty of measurements of the diameter of large particles by image analysis is relatively high, because the probability of cutting the larger particles through their centres is low. Secondly, the theoretical analysis assumes spherical particles whereas it can be seen (Fig. 6) that they are highly irregular. The irregular nature of the particles gives a larger surface area than a spherical particle of equivalent diameter, and thus led to a faster rate of increase of mass in the early stages of the experiment. This increased surface area only affects the initial mass increase, because the rate determining step for oxidation in this system is diffusion through the oxide, not gas–surface reactions. The overall effect of this is that the larger initial mass increase can be accommodated in the theory by the inclusion of fines in the calculated powder distribution.

4.4. Metallography and X-ray diffraction

The progress of the reaction was also monitored by metallography and X-ray diffraction (XRD) of partially and fully oxidized samples. A series of experiments at a nominal heating rate of 10 °C min^{-1} were stopped at temperatures of 330 °C (12% mass increase), 450 °C (13%), 600 °C (25%) and 840 °C (35%) for examination. In order to create enough reaction products for examination, these experiments used 0.5 g batches heated in a muffle furnace, spread out in a large 70 mm platinum crucible in order to minimize the pyrophoric effect. The mass increases given for these experiments are therefore not as accurate as the TGA experiments; however, X-ray diffraction of the large batches and similar TGA 20 mg samples showed that the same reactions were occurring. At 330 °C there is already considerable oxidation to a depth of approximately 1 to 2 μm (Fig. 11a), and XRD shows mainly a broad α-iron peak (Fig. 12). This is consistent with other investigations [8] which have found that low-temperature oxidation leads to the formation of a highly disturbed α-iron with finely dispersed hexagonal Nd_2O_3. There was no evidence of Nd_2O_3 in the X-ray diffraction patterns, probably due to the low volume fraction of Nd_2O_3 and the poor crystallinity of the oxidized powders. The gross cracking of particles shown in Fig. 11a are artefacts of mounting and polishing, because there was no preferential oxidation attack along the cracks. At 450 °C the low-temperature oxidation had consumed all but a few large particles (Fig. 11b), and another oxide layer was beginning to form. At 600 °C this secondary oxidation can be seen to consist of three distinct oxides (Fig. 11c), of progressively lighter coloration, going from the inside to the surface. The sequence of oxide colours is consistent with the oxidation of pure iron,

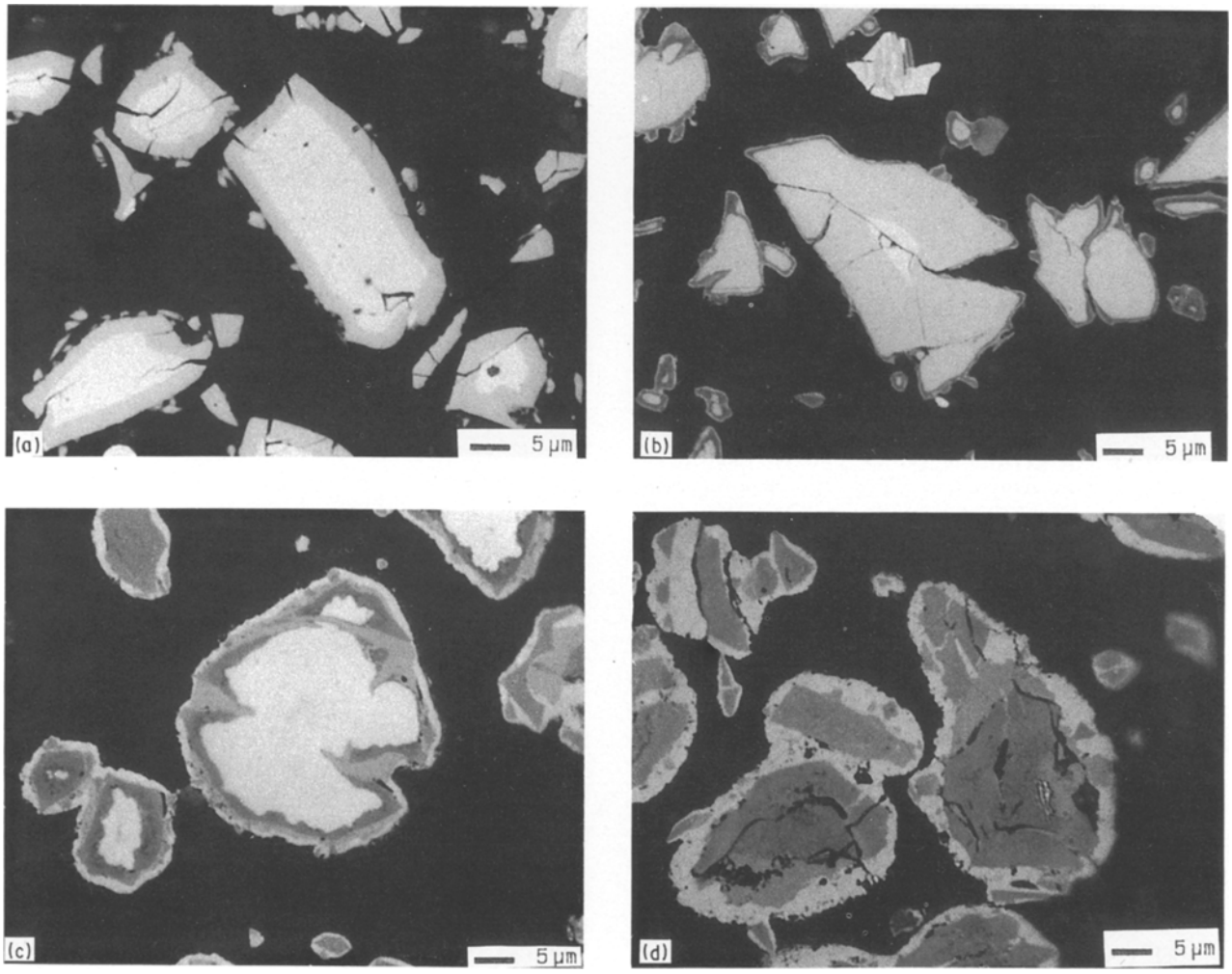

Figure 11 Optical micrographs of 10 °C min^{-1} experiment stopped at (a) 330 °C, (b) 450 °C, (c) 600 °C, (d) 840 °C.

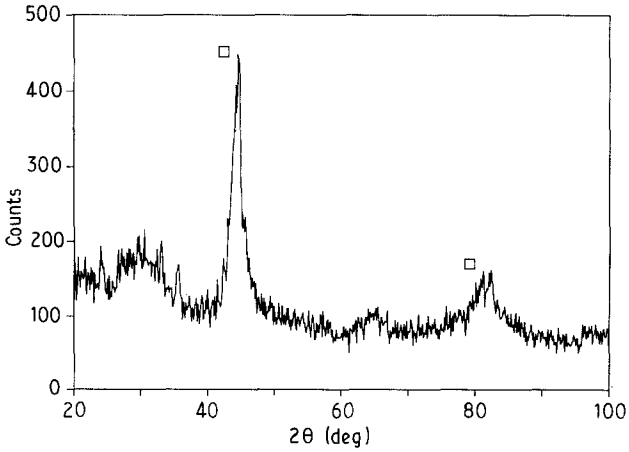

Figure 12 XRD of sample after isochronal oxidation, stopped at 330 °C. (□) Iron.

where the layers from the outside are Fe_2O_3, Fe_3O_4, and FeO. The presence of Fe_2O_3 and Fe_3O_4 was confirmed by X-ray diffraction; however, FeO was not detected, possibly due to insufficient X-ray penetration. In addition to optical examination, analytical electron microscopy using a windowless energy dispersive X-ray analyser was also performed. Fig. 13 shows the backscattered electron image and digital X-ray maps for oxygen, neodymium and iron for the test stopped at 600 °C. The oxygen map (Fig. 13a) shows the outer iron oxide region was much richer in oxygen than the inner neodymium oxide formed at low temperature. This is because there is more iron than neodymium present in the starting material, and not because of any difference in metal–oxide ratios. It is interesting to note that the neodymium map (Fig. 13b) and iron map (Fig. 13c) are not identical. Although the powders were nominally stoichiometric $Nd_2Fe_{14}B$ the isolated neodymium-rich, iron-poor particles indicates the material was not homogeneous. There has also been considerable diffusion of iron outwards, giving an iron-rich oxide covering an iron-depleted zone. The particles are therefore growing in size due to the outward diffusion of iron, while the neodymium remains immobile, thus the neodymium map marks the initial particle size. At 840 °C the interdiffusion has produced extensive porosity and the dominant oxides appear to be Fe_2O_3 and Fe_3O_4 (Fig. 11d); however,

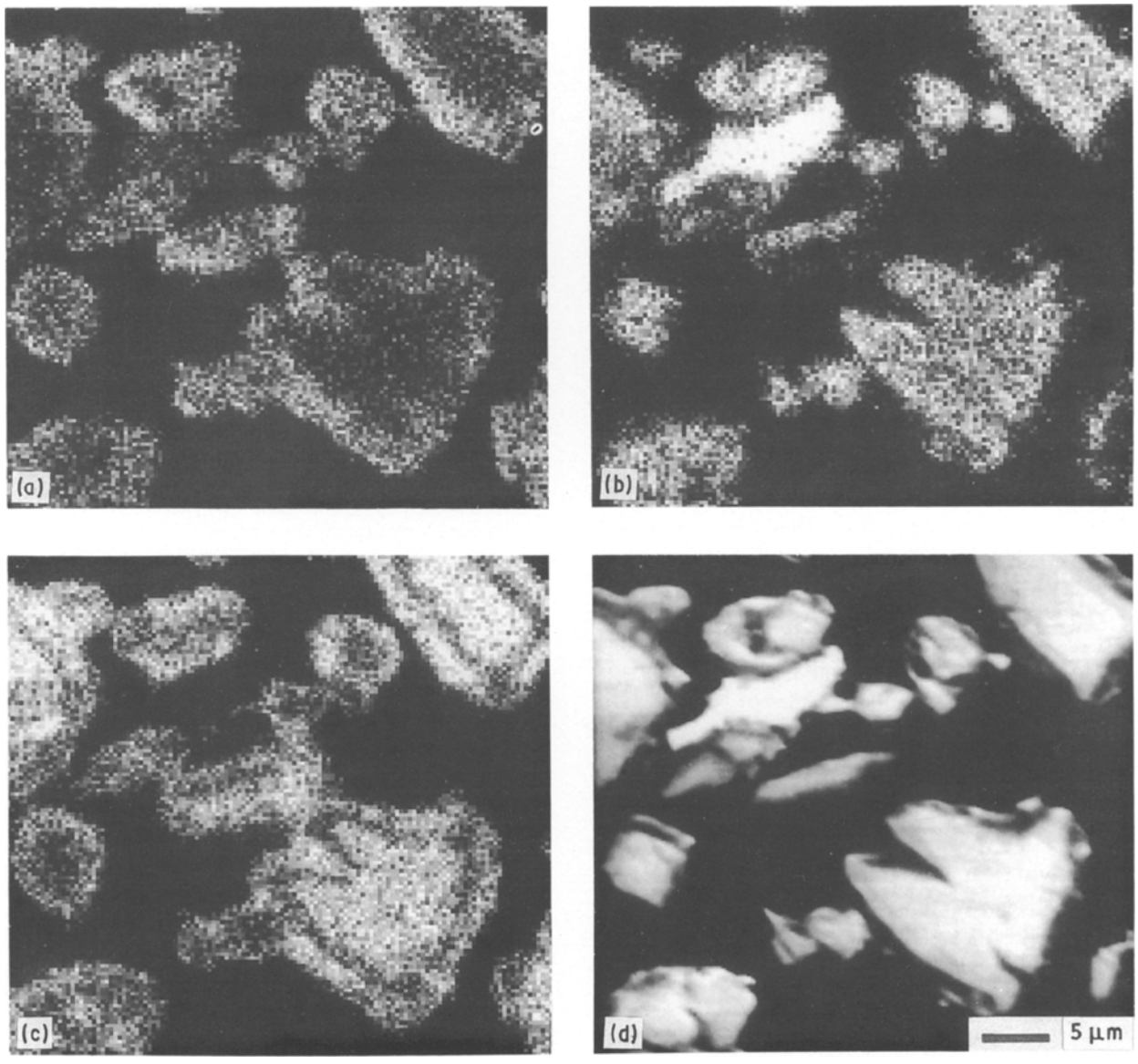

Figure 13 SEM images of samples in experiments stopped at 600 °C: (a) oxygen $K\alpha$, (b) neodymium $L\alpha$, (c) iron $K\alpha$, (d) backscattered electrons.

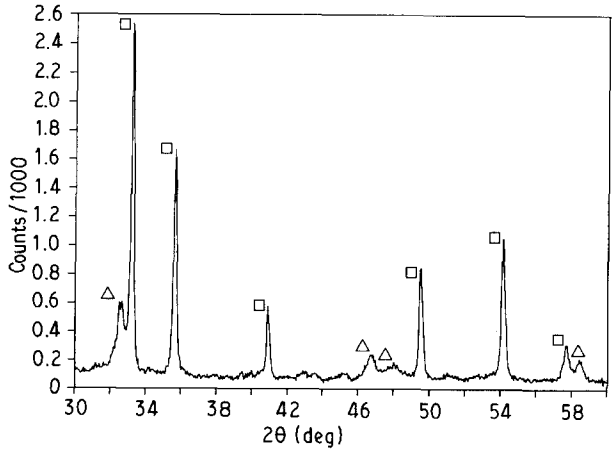

Figure 14 XRD of sample stopped at 840 °C. (□) Fe_2O_3, (△) $FeNdO_3$.

XRD of the powder even after prolonged ball milling shows only Fe_2O_3 and $FeNdO_3$ (Fig. 14). At this temperature, at a heating rate of 10 °C min^{-1}, the oxidation is largely complete, and the total mass change of approximately 35 wt % is consistent with the formation of oxides with a metal to oxygen atom ratio of 2:3.

It is clear from the structural examination that the oxidation of $Nd_2Fe_{14}B$ during sizing experiments is a two-stage process. At low temperature the neodymium oxidizes by the inward diffusion of oxygen, leaving iron dispersed with Nd_2O_3. It is not known what happens to the boron, because it could not be detected using SEM or by X-ray diffraction; however, given the low concentrations present we have assumed that it does not play a major role in scale formation. These particles then behave as pure iron, oxidizing by the outward diffusion of iron. The theory could accommodate the growth of particles, because this can be simulated by the inward growth of a depletion layer. However, two processes require two sets of oxidation parameters and the ratio of the mass change for the processes. The two-stage behaviour should be capable of being modelled by simply summing two curves, one for each process, weighted in the ratio of the oxide masses. Attempts to model behaviour on this basis proved unsuccessful due to the larger number of unknowns. However, the theory based on one process is simpler and fitted the experimental data reasonably well. Because the major part of the oxidation of $Nd_2Fe_{14}B$ is similar to that of pure iron, the activation energy of 100 kJ mol^{-1} derived from the sieving analysis was close to that determined in the iron powder experiments. The slightly lower value, and the inclusion of fines in the powder distribution are a result of the faster low-temperature oxidation of neodymium. The value of 50 kJ mol^{-1} for Q from the image analysis distribution must therefore be a consequence of the relative inaccuracy of the image analysis compared with the large sample size of oxidation sizing.

5. Conclusions

A particle sizing method developed for WC powders based on measurements of oxidation rate has been extended for use on iron and $Nd_2Fe_{14}B$ powders. On a narrow distribution of spherical iron particles the method compared favourably with image analysis of powders. The oxidation of $Nd_2Fe_{14}B$ powders consisted of two stages; below 400 °C, neodymium oxidized by the inward diffusion of oxygen, and above this temperature the particles essentially behave as pure iron, growing in size as iron diffused outwards. Powder sizing of $Nd_2Fe_{14}B$ proved more difficult than for WC because of this two-stage process and due to the wide size distribution and irregular shape of the powders examined. A disadvantage of the oxidation sizing technique is the need to know the parameters governing the kinetics of oxidation of the material to be sized. Alternatively a calibration experiment can be performed testing a sample of known size distribution. Thus, the accuracy of the method depends on the accuracy of the measurements of this distribution, and obtaining a definitive size distribution for the $Nd_2Fe_{14}B$ powders proved difficult. However, the technique can easily be used for fingerprinting powders, and due to its large sample size (greater than one million particles) is likely to be more representative than image analysis of a few hundred particles.

Acknowledgements

The stoichiometric $Nd_2Fe_{14}B$ powders were provided by Professor I. R. Harris, University of Birmingham. This paper is published by permission of the Controller of Her Majesty's Stationery office © Crown Copyright.

References

1. B. ROEBUCK, E. G. BENNETT, E. A. ALMOND and M. G. GEE, *J. Mater. Sci.* **21** (1986) 2033.
2. B. ROEBUCK, E. A. ALMOND and J. L. F. KELLIE, in "Horizons of Powder Metallurgy, PM86", Part 1, European Powder Metallurgy Federation, Dusseldorf, July 1986, edited by W. A. Kaysser and W. J. Huppmann (Verlag Schmid, Freiburg, Germany, 1986) pp. 123–6.
3. B. E. HIGGINS and H. OESTERREICHER, *IEEE Trans. Magn.* **23**(1) (1987) 92.
4. R. BLANK and E. ADLER, in "Proceedings of the 9th International Workshop on Rare Earth Magnets and their Applications", Bad Soden, FRG, September 1987, edited by C. Herget and R. Poerschke (University of Daytona, School of Engineering, 1987) pp. 537–44.
5. M. STEWART, M. G. GEE and B. ROEBUCK, in "Concerted European Action on Magnets (CEAM)", edited by I. V. Mitchell, J. M. D. Coey, D. Givord, I. R. Harris and R. Hanitsch (Elsevier Applied Science, London, 1989) pp. 532–42.
6. E. E. UNDERWOOD, "Quantitative Stereology" (Addison Wesley, Reading, Massachusetts, 1970) pp. 117–33.
7. O. KUBACHEWSKI and B. E. HOPKINS, "Oxidation of Metals and Alloys" (Butterworths, London, 1962) pp. 108–14.
8. P. SCHREY, *IEEE Trans. Magn.* **22**(5) (1986) 913.

Received 12 February
and accepted 26 February 1990